

# Material-Specific Phenomena and Developing Higher Yield Process Parameters in Selective Laser Melting of 17-4 PH Stainless Steel

EVREN YASA (✉ [ebalyasa@gmail.com](mailto:ebalyasa@gmail.com))

Eskişehir Osmangazi University <https://orcid.org/0000-0001-5443-3598>

İlker Atik

TÜBİTAK SAGE, Ankara

İpek Kandemir

TÜBİTAK SAGE, Ankara

---

## Research Article

**Keywords:** 17-4 PH Stainless Steel, Selective Laser Melting, Productivity, Double Yield

**Posted Date:** June 1st, 2021

**DOI:** <https://doi.org/10.21203/rs.3.rs-428820/v1>

**License:** © ⓘ This work is licensed under a Creative Commons Attribution 4.0 International License. [Read Full License](#)

---

# Abstract

Although Selective Laser Melting has become attractive in industrial applications seeking a high geometrical complexity with short lead times and customization, some bottlenecks still exist for wider adoption. Build rate is one of them while the high number of process parameters and their interactions easily exceeding hundreds which affects the part performance is the second. The machine manufacturers supply parameter sets generally optimized for maximum density leading to good mechanical properties. However, other factors need to be considered in process development. This study aims at increasing the build rate of at least 2 times for 17-4 PH stainless steel without any significant effect on the density, surface quality, material composition, mechanical properties and residual stresses. The results show an excessive ultimate tensile strength to yield strength ratio in comparison to reported literature which is attributed to the double yield phenomenon mainly attributed to the phases present in the microstructure as a result of powder chemical composition and processing gas. Thus, it is concluded that powder chemical composition and processing gas are much more effective on the outcome while the process parameters with an increased build rate do not significantly change the results provided that almost full density is reached.

## 1. Introduction

Selective Laser Melting (SLM) is one of the very advantageous AM processes for metallic materials in comparison to subtractive manufacturing due to its ability to create highly complex geometries, low amount of waste material, reduced lead time from design to testing, simplified supply chains, decreased number of joining processes possibly leading to an improved part life, etc. Moreover, unlike conventional manufacturing, the SLM process does not necessitate design of special tools / molds and directly starts from the CAD file of the part to be produced as shown in Fig. 1. SLM has recently been increasingly adopted for manufacturing functional end-parts in diverse demanding industries such as aerospace, defence and biomedical. However, to explore the full potential of SLM, some barriers still need to be overcome. One of the very important limitations is the high number of process parameters that affect the part performance as well as the low build rate. The process parameters do not only have direct influence on the part performance but also their interactions due to the physical phenomena occurring during the SLM process play a significant role on the outcome. Although the machine vendors generally provide or sell an initial set of process parameters optimized for each material, these may be far from optimum when multiple criteria are taken into account. Generally, the given process parameters are optimized taking density into consideration since mechanical properties severely deteriorate if excessive porosity is present. However, due to inherent nature of the SLM process, other criteria become dominant on the part performance as well. For example, due to the high cooling rates encountered in the process, residual stresses leading to part deformations or even cracks during the process become one of the problems. Moreover, especially for internal features, it is generally difficult to improve the surface quality after the process is completed. Without reaching the desired levels of surface roughness, the advantage of creating very complex geometries stays limited. Thus, as-built surface roughness is also critical. Moreover, productivity needs to be taken into account as one of the bottlenecks of SLM. The productivity, which can be expressed in terms of build rate, depends on many factors such as material properties, machine/laser configuration (multiple lasers, bi-directional powder coating, etc.), part orientation, scanning parameters and nesting. Additionally, the selected layer thickness is very critical in terms of the build rate due to its direct effect on the number of layers.

In the last decade, the SLM studies on the 17 – 4 PH stainless steel (SS) in the literature have been increased. Murr et al. has presented one of the most comprehensive studies on the SLM of this material studying martensitic or mostly austenitic phase powders which were produced by atomization in argon or nitrogen, respectively. Those powders were then used in the SLM process using Ar or N<sub>2</sub> atmospheres. It was concluded that the phase in the

final part is the same as the powder phase (austenitic or martensitic) when  $N_2$  is utilized. The final parts exhibit a martensitic structure with either an austenitic or martensitic pre-alloyed 17 – 4 PH SS powder provided that argon is used in the SLM [1]. Auguste et al. have investigated powder batches from different suppliers and applied various heat treatments. They concluded that the chemical composition of different powder batches leads to different phases in the end, one being mostly ferritic while the other being mostly martensitic leading to different mechanical properties [2]. On the other hand, the studies involving optimizing process parameters for the SLM of 17 – 4 PH SS are quite limited. Mahmoudi et al. have investigated the mechanical properties and microstructural characterization to understand the effect process parameters including build orientation as well as thermal history and applied heat treatment. However, the process parameters were only studied as “default and optimized” sets without giving any further information [3]. In another study by Hu et al., the effect of scan speed, hatch distance and layer thickness was studied with single factor experiments on the density and microhardness [4].

Although  $N_2$  is often used in the gas-atomization of stainless steels, it is not inert. In addition to its role to stabilize the FCC (face-centered cubic) austenite phase, it substitutes for C in various carbide phases leading to the formation of other carbide/nitride phases, similar to C [5]. Moreover, during the SLM process, the lower conductivity of argon in comparison to nitrogen leads to martensitic products from either austenitic or martensitic 17 – 4 PH SS powder [3]. In addition to the processing gas, the material composition of the powder has a significant impact on the final parts’ microstructure and thus mechanical properties for 17 – 4 PH [2, 6, 7]. The  $Cr_{eq}/Ni_{eq}$  value calculated by WRC-1992 equation varies based on the volume fraction of residual delta-ferrite. The study by Vunnam et al. has concluded that a lower  $Cr_{eq}/Ni_{eq}$  value results in martensite formation and a less retained delta-ferrite after the SLM process [7].

The difference in mechanical properties obtained with SLM in comparison to conventional manufacturing is generally attributed to the layerwise nature of the process leading to finer and elongated grains as well as high cooling rates. However, the difference in the 17 – 4 PH SS cannot be only explained with grain refinement due to high cooling rates. Some researchers point out the presence of a high volume fraction of retained austenite within the martensitic alloy leading to significant difference in resulting mechanical properties [9]. In the literature, the range of retained austenite severely changes from 5–95% although using very similar process parameters generally optimized for maximum density. The factors influencing the amount of retained austenite have only partially been addressed in the literature. AlMangour and Yang has concluded that fine grains led by the rapid cooling rates of the SLM process reduces the austenite to martensite formation ( $M_s$ ) temperature [10]. Additionally, a high nitrogen content in the material composition coming from the gas atomization can further reduce this temperature [11]. This leads to a significant volume fraction of retained austenite in the as-built material at room temperature. During deformation, due to its being a metastable phase, the retained austenite transforms to martensite bringing an additional complication with respect to measurement of retained austenite fractions. This is due to the fact that some sample preparation methods may result in local deformations and consequent martensite formation at the surface [12]. By applying a heat treatment above austenite transition temperature, the volume of retained austenite can be reduced by transforming into martensite [13]. It is not easy to control the cooling rate in SLM by simply changing the process parameters. This is also demonstrated in the study by Gu et al., which addressed the change of the amount of retained austenite by varying laser power and speed [13]. It shall also be noted that XRD data may not be sufficient to differentiate the martensite having a body centered tetragonal (BCT) structure and BCC ferrite phase. This is mainly due to very low magnitude of the lattice distortion in the martensite in stainless steels having a C level smaller than 0,02 wt.% [7]. This necessitates the use of EBSD for phase differentiation.

Table 1 summarizes the reported work for the obtained microstructure/mechanical properties of the as-built specimens from 17 – 4 PH SS. The variability in the reported microstructures and obtained mechanical properties is much higher when compared to other materials used in SLM. The hardness values range from approximately 150 to 350 HV while reported tensile properties exhibit a high scatter as shown in Fig. 2 mainly depending on their microstructure. UTS/YS ratios change from 1 to 2 in different studies.

Table 1

Comparison of various studies on SLM of 17 – 4 PH Stainless Steel (approximate values are given for some data)

Ref.	Atomization Gas	Processing Gas	Mat. Comp. Ratio (Cr)eq/(Ni)eq	Hardness [HV]	Microstructure	Tens. Prop. UTS/YS Elongation
[1]	Argon	Argon	Not given	30 HRC	Completely martensitic	Not given
[1]	Nitrogen	Argon	Not given	32 HRC	Completely martensitic	Not given
[1]	Nitrogen	Nitrogen	Not given	22 HRC	Austenitic components with roughly 15% martensite	Not given
[2]	Not given	Argon	SLM 2,04	330 HV	Mainly martensitic	1100/500
[2]	Not given	Argon	TLS 2,41	300 HV	Ferritic with martensitic structure and retained austenite	900/850
[3]	Not given	Argon	3D Systems SLM powder	300–350 HV	Depending on the dwell time, the volume fraction of austenite 13–26%.	950/650 1050/625
[4]	Not given	Argon	Hengji (10–74 μm)	260 ± 20 HV	Alpha and gamma phases present	1100/640
[5]	Nitrogen	Nitrogen	EOS StainlessSteel GP1	Not given	A significant fraction of retained austenite in the as-built condition, > 90 %	Not given
[6]	Not given	Argon	Powder1 (d90 < 16μm)	278 ± 57 HV	Alpha phase 38% vol. Gamma phase 62% vol.	880/614
[6]	Not given	Argon	Powder2 (d90 < 25μm)	226 ± 69 HV	Alpha phase 6% vol. Gamma phase 94% vol.	Not given
[7]	Argon		Powder A 2,76	277.3 ± 10 HV	Columnar grains, small martensitic laths	763/607 22.3 ± 0.7 %
[7]	Argon		Powder B 2,65	330.7 ± 9 HV		871/699 19.4 ± 1.0 %
[7]	Argon		Powder C 2,43	333.0 ± 5 HV	A fine grain microstructure	917/723 10.9 ± 0.9 %
[8]	Argon	Not given	Powder A 3,88	Not given	Ferritic grains and visible martensitic grain structures	900 MPa XY 800 MPa Z
[8]	Argon	Not given	Powder B Ar 3,89	Not given	Ferritic grains	900 MPa XY 800 MPa Z

Ref.	Atomization Gas	Processing Gas	Mat. Comp. Ratio (Cr)eq/(Ni)eq	Hardness [HV]	Microstructure	Tens. Prop. UTS/YS Elongation
[8]	Nitrogen	Not given	Powder B N2 3,41	Not given	Large ferrite grains accompanied by a fine and equiaxed austenite grains	1050
[8]	Argon	Not given	Powder C-3,31	Not given	Contains largely martensite	1050
[12]	Argon	Argon	2.77	380 HV	72% austenite, 28% martensite	1300/600
[13]	Nitrogen	Argon	EOS	Not given	More than 96% austenitic	Not given
[13]	Nitrogen	Nitrogen	EOS	Not given	Completely austenite	Not given
[13]	Argon	Argon	LPW	Not given	Mostly martensite	Not given
[13]	Argon	Nitrogen	LPW	Not given	Mostly martensite	Not given
[15]	Nitrogen	Nitrogen		310 HV	Mostly martensite	Not given

## 2. Materials And Methods

The used powder material was obtained from SLM Solutions having almost spherical particles with some minor satellites. For density evaluations, cubic specimens having dimensions of 15x15x15 mm were built on an SLM Solutions SLM 280 machine under nitrogen as protective atmosphere using a scan strategy of stripe scanning. The layer thickness was doubled in comparison to the initial set of parameters and kept constant at 60 µm while the effects of the laser power (200-275-350 W), scan speed (600-800-1000-1200 mm/s) and hatch distance (0.09-0.12-0.15 mm) were tested with a full factorial test strategy. After the production was complete, the specimens' densities were measured by the Archimedes' method taking the reference density as 7.8 g/cm<sup>3</sup> while the surface quality was assessed by Mitutoyo SJ-310 surface profilometer. Some parameters sets from the first batch leading to the lowest porosity values yielding a good level of build rates were identified and new specimens were produced in the second batch to test the hardness, tensile properties and deformations due to residual stresses as well as to investigate the material composition and microstructural features in comparison to initial parameter set with 30 µm of layer thickness (see Table 2). The tensile properties were tested per EN 2002-001: 2005 while the bridge curvature method (BCM) was used to quantitatively compare the deformations led by the residual stresses after the parts were removed from the base plate [18]. The microhardness tests were accomplished on with a loading of 1 kgf. Optical Microscopy (OM) and Scanning Electron Microscopy (SEM) were used to reveal the microstructural defects and features. The specimens were firstly etched with Vilella's reagent for microstructural investigation and then electro-etched to clearly observe melt pool boundaries. The chemical compositions were obtained by spectral analysis on Spectromax and compared to the values specified in ASTM A564 while the EBSD analysis was carried out on a QUANTA 400F Field Emission SEM.

Table 2  
The tested parameter sets in the second batch

Par. Set #	Layer Thickness [ $\mu\text{m}$ ]	Scan Speed [ $\text{mm/s}$ ]	Laser Power [W]	Hatch Distance [ $\mu\text{m}$ ]
B2-St-30	30	800	200	120
B2-1-30	30	1000	350	150
B2-2-60	60	1000	350	150
B2-3-60	60	1000	350	120
B2-4-60	60	1200	275	90

### 3. Results And Discussion

#### 3.1 Density Results

The relative density results of the first batch specimens range from 86–99.5% for parameters using a layer thickness of 60  $\mu\text{m}$  whereas the initial parameter set for a layer thickness of 30  $\mu\text{m}$  leads to a density result of 99.8%. The variation of the relative density with respect to the scan speed at different laser power and hatch distance values are depicted in Fig. 3 with corresponding trend lines and  $R^2$  values. In Fig. 3a where a hatch distance of 90  $\mu\text{m}$  is used meaning that consecutive scan lines are closely placed, very low porosity values are obtained. All parameter sets with a hatch distance of 90  $\mu\text{m}$  led to a porosity of less than 1% except the one with the lowest energy density (200 W laser power, 1200 mm/s scan speed). In Fig. 3b where a hatch distance of 120  $\mu\text{m}$  is used, it is seen that when the linear energy density (the ratio between the laser power and scan speed) is sufficiently high, good densities above 99% can be obtained. However, as the linear energy density is lowered then the porosity values start to increase as demonstrated with a laser power of 200 W giving the lowest energy density in the tested range for Fig. 3b. The effect of lowering the laser power is more pronounced when the hatch distance is set to 150  $\mu\text{m}$  meaning that the consecutive laser lines are sparsely placed in comparison to other values as demonstrated in Fig. 3c.

Since the aim of this study is to increase the build rate by doubling the layer thickness, the relative densities with respect to the indicative build rates, calculated as the multiplication of the scan speed, hatch distance and layer thickness, are presented in Fig. 4. The initial parameter set with a layer thickness of 30  $\mu\text{m}$  gives the highest density at a rather low build rate, i.e. 4.3  $\text{mm}^3/\text{s}$ , as shown. Most of the parameter sets utilizing a high laser power (275–350 W) give a density above 99% up to an indicative build rate of 8.6  $\text{mm}^3/\text{s}$ . However, reducing the laser power to 200 W almost totally eliminates high densities above 99% with high build rates.

#### 3.2 Microhardness and Residual Stresses

As a result of the first batch aiming to identify the suitable parameter sets to provide increased build rates without significantly changing the density, the parameter sets with a layer thickness of 60  $\mu\text{m}$  given in Table 2 are selected for further testing as well as two sets of reference parameters with a layer thickness of 30  $\mu\text{m}$ . The measured microhardness values with these parameter sets are presented in Table 3. It can be concluded that the variation of the process parameters does not significantly alter the obtained microhardness results. Moreover, they are very high in comparison to other reported hardness test results (see Table 1).

Table 3  
The results obtained with the tested parameter sets in the second batch

Parameter set #	Layer Thickness [μm]	Scan Speed [mm/s]	Laser Power [W]	Hatch Distance [μm]	Relative Density [%]	Indicative Build Rate [mm <sup>3</sup> /s]	Microhardness [HV]	BCM Deviation [°]
B2-St-30	30	800	200	120	99,81%	2,9	355,7 ± 6,7	0,16
B2-1-30	30	1000	350	150	99,74%	4,5	362,7 ± 8,7	0,15
B2-2-60	60	1000	350	150	99,65%	9,0	344,0 ± 6,9	0,14
B2-3-60	60	1000	350	120	99,49%	7,2	368,0 ± 2,7	0,28
B2-4-60	60	1200	275	90	99,48%	6,5	362,7 ± 5,7	0,21

It is well known that different heat inputs may lead to different levels of residual stresses in the SLMed parts. As a fast and easy method enabling qualitative comparisons, BCM is utilized in this study. When the bridge geometry is produced on the base plate, it is cut off by wire electro discharge machining (WEDM), it is curled up because of the relaxation of the residual stresses. By measuring this angle of curling using the planes at the bottom of the bridge, a quantitative indicator is obtained. The curling angles with different process parameter sets are shown in Table 3 in the last column. Although some parameters lead to a smaller angle, all measured angles are very low in comparison to other curling angles obtained in other studies in the literature [15, 17]. For example, the standard parameter set in [18] led to a curling angle of 1,3° for AISI 316L stainless steel whereas the maximum curling angle in this study is only limited to 0,28°. Thus, it is concluded that changing the layer thickness and increasing the productivity does not significantly change the residual stresses in the part within the tested range.

### 3.3 Material Composition

It is observed that the change of the process parameters does not influence the chemical composition of the produced specimens according to the spectral analysis results per ASTM A564 as presented in Table 4. Regarding the elements of C, S, O and N, LECO analytical elemental analysis was performed per ASTM E 1019. Each specimen was measured three times and the average of these measurements were taken to check its conformity per specifications. It is seen that none of the tested parameter sets lead to non-conformance as shown in Table 5.

Table 4  
The results of the spectral analysis of specimens produced in the second batch

		<b>B2-St-30</b>	<b>B2-1-30</b>	<b>B2-2-60</b>	<b>B2-3-60</b>	<b>B2-4-60</b>
C	Max 0,07%	0,04%	0,04%	0,04%	0,04%	0,04%
Si	Max 1%	0,70%	0,69%	0,68%	0,68%	0,70%
Mn	Max 1%	0,37%	0,37%	0,39%	0,40%	0,39%
P	Max 0,040%	0,01%	0,01%	0,01%	0,01%	0,01%
S	Max 0,030%	0,00%	0,00%	0,01%	0,00%	0,01%
Cr	15–17,5%	15,51%	15,54%	15,56%	15,55%	15,52%
N	Max 0,10%	0,08%	0,07%	0,07%	0,07%	0,07%
Fe	Balanced	74,60%	74,50%	74,40%	74,40%	74,50%
Ni	3–5%	4,26%	4,24%	4,21%	4,24%	4,22%
Cu	3–5%	4,09%	4,13%	4,21%	4,20%	4,18%
Nb	0,15 – 0,45%	0,17%	0,16%	0,16%	0,16%	0,17%
Ta		< 0,02%	< 0,02%	< 0,02%	< 0,02%	< 0,02%

### 3.4 Microstructural Investigations (SEM, OM)

The microstructures of the specimens produced within the second batch are investigated. As shown in Fig. 5, the microstructures with 30 µm layer thickness do not contain any residual pores. The etched micrographs indicate that the melt pool depths are much higher than the selected layer thickness shown with yellow lines. A higher laser power with B2-1-30 having the same layer thickness in contrast to B2-St-30 leads to much deeper and narrower melt pools.

In Fig. 5, the optical micrographs with 60 µm of layer thickness are also demonstrated with different parameter sets. The ratio of the melt pool depth to the layer thickness in these parts is smaller compared to parts made with a layer thickness of 30 µm. However, as shown in the micrographs, there is a good fusion between the consecutive tracks and layers leading to a very small amount of porosities. However, with B2-4-60, some big and irregular pores due to lack of fusion are visible. The lack of fusion porosity is evident from irregular shape and pores filled with unmelted powder particles.

Table 5

The results of analytical elemental analysis for C,S,O, N and H with LECO elemental analysis equipment

Parameter set #	C [wt.%]	S [wt.%]	O [wt.%]	N [wt.%]	H [wt.%]
B2-St-30	0,0525	0,0039	0,0501	0,0811	0,0006
B2-1-30	0,0444	0,0042	0,0448	0,0769	0,0004
B2-2-60	0,0523	0,0045	0,0714	0,0815	0,0004
B2-3-60	0,0457	0,0039	0,0557	0,0803	0,0004
B2-4-60	0,0446	0,0041	0,0431	0,0772	0,0004
Spec. per ASTM A 564/A 564M[20]	Max. 0,07	Max. 0,03	-	-	-
Spec. per SLM Solutions for powder [22]	0,07	0,015	0,04	0,10	-

One of the other remarkable features of the optical microscopy images given in Fig. 5 is the darker areas at the deep end of the melt pools close to the boundary. Although these dark areas can be confused with porosity in the etched versions, a closer look into these areas reveal that these regions have very dense cellular structures (see Fig. 6a-b). The cell size is very small being below 1  $\mu\text{m}$  and the cells mostly have a homogenous size distribution as depicted in Fig. 6c. The SEM images shown in Fig. 6 demonstrate some white areas. In order to understand the source of these white areas, EDS analysis was performed on B2-2-60 and B2-St-30 specimens. The results show that these are mainly iron carbides as depicted in Fig. 7. This is consistent with the results of some other studies finding non-metallic inclusions in the SLM 17 – 4 PH SS [19, 20].

The results of the EBSD analysis of B2-St-30 and B2-2-60 are given in Fig. 8. The average fraction of ferrite is 39% and the one of austenite is 8,5% while the one of martensite is 52,5%. This is a different microstructure than wrought 17–4 PH steels which often have a fully martensitic microstructure. However, it is not uncommon to find some retained austenite in the microstructure due to the presence of  $\text{N}_2$  in both gas atomization and SLM processing as an austenite stabilizer. Moreover, the martensite finish temperature is slightly above the room temperature. Thus, very low variations in the material composition, even staying in the 17-4PH SS specification, can have a significant change on the microstructure regarding the phase composition. Inverse Pole Figures (IPF) given in Fig. 9 show that the specimens exhibits mixed grain structure having a columnar BCC grains parallel to the build direction with finer equiaxed FCC grains at melt pool boundaries. The IPF's for both of the specimens reveal similar structures. However, the main difference is much more elongated grains along the build direction in B2-2-60 specimen, mainly due to doubled layer thickness and much higher laser power.

Schaeffler diagram can be used to understand the phase evolution in 17 – 4 PH stainless steel [23]. In this study,  $\text{Cr}_{\text{eq}}$  is equal to 16,65 – 16,66 where as  $\text{Ni}_{\text{eq}}$  is calculated as 5,61 – 5,64. When these values are approximately marked on the diagram, the intersection point lies in the region of martensite + ferrite. However, there is some level of retained austenite 5–10% in the obtained microstructures. This may be due to the high cooling rates encountered in the SLM process not allowing fully austenite transformation.

### 3.5 Tensile Test Results and Fracture Surfaces

The results of the tensile tests are presented in Fig. 10 with 95% confidence intervals from 3 repetitions. It is evident from the figures that the average ultimate tensile strength (UTS) and yield strength (YS) values are a bit higher, namely 4% and 15% respectively, when a layer thickness of 30  $\mu\text{m}$  is used rather than 60  $\mu\text{m}$ . Regarding elongation at break, it can also be concluded that the confidence intervals indicate a smaller value when a thinner layer

thickness is preferred. An interesting observation of the tensile results is the high discrepancy between UTS and YS values. According to SLM Solutions Material Datasheet [22], the tensile strength for a layer thickness of 30  $\mu\text{m}$  shall be  $931 \pm 45$  MPa while the YS shall be  $506 \pm 25$  MPa as minimum. While the UTS values obtained in this study significantly exceeds the given threshold significantly, YS values are far below the given limit. A representative stress-strain curve from B2-2-60 specimen is shown in Fig. 11. The tensile test results show that there is a large discrepancy between YS and UTS. The obtained YS is much lower than expected whereas the UTS is higher than most of the reported values in the literature. This conclusion is valid for all tested parameter sets and independent from the layer thickness. One of the reasons of having a low YS values may be attributed to the selected strain rate. The strain rate, which was taken as mm/min appropriately per tensile testing standard, has shown to have a significant effect on the yield stress by Wang et al. [28]. Moreover, it is also reported that the phase transformation can be observed in martensitic PH stainless steels during deformation. This can lead to an increased UTS as a result of the transformation induced plasticity (TRIP) effect. As shown in Fig. 11, the phenomenon of having “double yield” in the stress-strain curve is thus attributed to the formation of strain-induced martensite and further strengthening during deformation. The number of studies showing this effect is very limited for additive manufacturing [29]. Moreover, the highest UTS/YS ratios found in literature for this material after SLM are about 2 whereas it is equal to almost 4 for this study emphasizing the importance of double yield phenomenon. A post-heat treatment to be applied after the SLM process before aging is thus recommended to eliminate the metastable austenite and to increase the yield strength.

SEM images of the tensile fracture surface of various specimens in the as-built condition are shown in Fig. 12. The shape of the fracture dimples in terms of size, depth and quantity, relies on the ductility of materials as well as the second phase particles [23]. The fracture surfaces of specimens having a layer thickness of 30  $\mu\text{m}$  reveal a cup-and-cone fracture. At high magnifications, micro-void coalescence fracture, which is also known as dimpled rupture, is observed. It is evident from the figures that porosity and unmelted powder particles, especially observed in B2-4-60, can act as nucleation sites for cracks under tensile loading. Additionally, during loading in tensile testing, void nucleation can stem from cracking of particle–matrix interfaces for both secondary phases and unmelted particles. The co-existing deep holes, which are present in all samples can be attributed to molten liquid shrinkage or vaporization. The deep holes resemble holes observed with other materials in AM which reveal brittle rod-like intergranular fracture of dendrites [27].

## 4. Conclusions

This study aims at identifying a new process parameter set for an increased productivity by doubling the layer thickness while not affecting the residual stresses, material composition and mechanical properties. Starting from an initial set of parameters optimized for a layer thickness of 30  $\mu\text{m}$  for 17 – 4 PH stainless steel, a wide range of various scan speed, laser power and scan spacing was tested for a layer thickness of 60  $\mu\text{m}$ . Some of the tested parameters giving a high density above 99,5% and leading to a build rate increase of 2–3 times in comparison to initial set of parameters were tested in terms of hardness, material composition, tensile properties, residual stresses and microstructure.

The results within the tested ranges show that

- The variation of the process parameters does not significantly alter the obtained microhardness results.
- Using the bridge curvature method, changing the layer thickness and increasing the productivity does not significantly change the residual stresses in the part.

- None of the tested parameter sets lead to non-conformance in terms of material composition although a very high laser power is utilized for thick layers.
- A hierarchical microstructure is obtained with a cellular structure having a cell size below 1  $\mu\text{m}$ .
- Although wrought 17–4 PH steels which usually have a fully martensitic (BCC) microstructure, it is observed that 5–10% retained austenite is present in the microstructure while the ferritic and martensitic phases are found in fractions of 41% and 51%, respectively. This can be considered as independent from the utilized process parameters.
- Tensile test results reveal a very high ultimate tensile strength and low yield strength in comparison to reported values for SLM 17 – 4 PH stainless steel with a specific “double yield” behaviour. This can be attributed to the strain induced hardening during tensile testing due to reversion of retained austenite to martensite. This is a very important outcome from this study as an important point to clarify the wide scatter of mechanical properties from this alloy processed by SLM. The phases and their fractions highly depend on the powder chemical composition ( $\text{Cr}_{\text{eq}}/\text{Ni}_{\text{eq}}$  ratio) and processing gases used in atomization and SLM process. Thus, a solution annealing is recommended to manage the microstructure before aging for this material as a post-processing step after SLM.

## Declarations

### Funding

This research did not receive any specific grant from funding agencies in the public, commercial, or not-for-profit sectors.

### Conflict of Interest / Competing Interests

The authors declare that they have no known competing financial interests or personal relationships that could have appeared to influence the work reported in this paper.

### Availability of data and material

All data generated or analysed during this study are included in this published article.

### Code availability

Code sharing not applicable to this article as no codes were generated during the current study.

### Authors' contributions

All authors contributed to the study conception and design. Production, material preparation and characterization as well as the analysis of results were performed by Evren Yasa, İlker Atik and İpek Kandemir. The first draft of the manuscript was written Evren Yasa and all authors commented on previous versions of the manuscript. All authors read and approved the final manuscript.

### Ethics approval

This paper/study does not contain any studies with human participants or animals performed by any of the authors.

## Consent to participate

Not applicable since this paper/study does not contain any studies with human participants performed by any of the authors.

## Consent for publication

Not applicable since this paper/study does not contain any studies with human participants performed by any of the authors.

## References

1. Murr LE, Martinez E, Hernandez J, Collins S, Amato KN, Gaytan SM, Shindo PW (2012) Microstructures and Properties of 17-4 PH Stainless Steel Fabricated by Selective Laser Melting. *Journal of Materials Research and Technology* 1/3: 167–77. doi:10.1016/S2238-7854(12)70029-7.
2. Auguste P, Mauduit A, Fouquet L, Pillot S (2018) Study on 17-4 PH stainless steel produced by selective laser melting. *UPB Scientific Bulletin, Series B: Chemistry and Materials Science* 80: 197-210.
3. Mahmoudi M, Elwany A, Yadollahi A, Thompson SM, Bian L, Shamsaei, N (2017) Mechanical properties and microstructural characterization of selective laser melted 17-4 PH stainless steel. *Rapid Prototyping Journal* 23/2: 280-294.
4. Hu Z, Haihong Z, Zhang H, Zeng X (2017) Experimental investigation on selective laser melting of 17-4PH stainless steel. *Optics & Laser Technology* 87: 17-25.
5. Lass EA, Zhang F, Campbell CE (2020) Nitrogen Effects in Additively Manufactured Martensitic Stainless Steels: Conventional Thermal Processing and Comparison with Wrought. *Metallurgical and Materials Transactions A* 51: 2318–2332.
6. Averyanova M, Bertrand P, Verquin B (2010) Effect of initial powder properties on final microstructure and mechanical properties of parts manufactured by selective laser melting. *Annals of DAAAM for 2010 & Proceedings of the 21st International DAAAM Symposium 21, No. 1: ISSN 1726-9679.*
7. Vunnam S, Saboo A, Sudbrack C, Starr TL (2019) Effect of powder chemical composition on the as-built microstructure of 17-4 PH stainless steel processed by selective laser melting. *Additive Manufacturing* 30: 100876.
8. Dobson S, Vunnam S, Frankel D, Sudbrack C, Starr T (2019) Powder variation and mechanical properties for SLM 17–4PH stainless steel in Proc. of Solid Freeform Fabrication Symposium, Austin, TX, USA.
9. Coulson S (2018) Analysis of Additively Manufactured 17-4PH Stainless Steel, Master of Applied Science thesis, McMaster University.
10. AlMangour B, Yang J-M (2017) Understanding the Deformation Behavior of 17-4 Precipitate Hardenable Stainless Steel Produced by Direct Metal Laser Sintering Using Micropillar Compression and TEM. *The International Journal of Advanced Manufacturing Technology* 90/1–4: 119–26.
11. Rafi HK, Pal D, Patil N, Starr TL, Stucker BE (2014) Microstructure and Mechanical Behavior of 17-4 Precipitation Hardenable Steel Processed by Selective Laser Melting. *Journal of Materials Engineering and Performance* 23, no. 12: 4421–28.
12. Facchini L, Vicente N, Lonardelli I, Magalini E, Robotti P, Alberto M (2010) Metastable Austenite in 17-4 Precipitation-Hardening Stainless Steel Produced by Selective Laser Melting. *Advanced Engineering Materials*

- 12, no. 3: 184– 88.
13. Starr T, Rafi K, Stucker B, Scherzer C (2012) Controlling Phase Composition in Selective Laser Melted Stainless Steels in Proc. of Solid Freeform Fabrication Symposium, Austin, TX, USA.
  14. Gu H, Gong H, Pal D, Rafi K, Starr T, Stucker B (2013) Influences of Energy Density on Porosity and Microstructure of Selective Laser Melted 17- 4PH Stainless Steel in Proc. of Solid Freeform Fabrication Symposium, Austin, TX, USA.
  15. Leo P, D'Ostuni S, Perulli P, Sastre MAC, Fernández-Abia AI, Barreiro J (2019) Analysis of microstructure and defects in 17-4 PH stainless steel sample manufactured by Selective Laser Melting. *Procedia Manufacturing* 41: 66-73.
  16. Hajnys J, Pagáč M, Měsíček J, Petru J, Król M (2020) Influence of Scanning Strategy Parameters on Residual Stress in the SLM Process According to the Bridge Curvature Method for AISI 316L Stainless Steel. *Materials* 13, no. 7: 1659.
  17. Vrancken B (2016) Study of Residual Stresses in Selective Laser Melting, PhD diss., Catholic University of Leuven.
  18. Kruth J-P, Deckers J, Yasa E, Wauthlé R (2012) Assessing and comparing influencing factors of residual stresses in selective laser melting using a novel analysis method. *Proc. of the Institution of Mechanical Engineers, Part B: Journal of Engineering Manufacture* 226, no. 6: 980-991.
  19. Sun Y, Hebert RJ, Aindow M (2018) Effect of heat treatments on microstructural evolution of additively manufactured and wrought 17-4PH stainless steel. *Materials & Design* 156, 429-440.
  20. Sun Y, Aindow M., Hebert R (2017) Microstructural Study of the Heat-treated 17-4PH Stainless Steel Parts Prepared by Selective Laser Melting. *Microscopy and Microanalysis* 23, 2252-2253
  21. ASTM A 564/A 564M – 04 Standard Specification for Hot-Rolled and Cold-Finished Age-Hardening Stainless Steel Bars and Shapes
  22. SLM Solutions 17-4 PH material datasheet. [https://www.slm-solutions.com/fileadmin/Content/Powder/MDS/MDS\\_Fe-Alloy\\_17\\_4PH\\_1219\\_EN.pdf](https://www.slm-solutions.com/fileadmin/Content/Powder/MDS/MDS_Fe-Alloy_17_4PH_1219_EN.pdf)
  23. Wang Q, Zhang S, Zhang C, Wu C, Wang J, Chen J, Sun Z (2017) Microstructure evolution and EBSD analysis of a graded steel fabricated by laser additive manufacturing. *Vacuum* 141: 68-81.
  24. Schaeffler AL (1949) Constitution Diagram for Stainless Steel Weld Metal, *Metal Prog.* 56, no. 11: 680.
  25. Brandi SD, Schön CG (2017) A Thermodynamic Study of a Constitutional Diagram for Duplex Stainless Steels. *Journal of Phase Equilibria and Diffusion* 38: 268–275
  26. Lin X, Cao Y, Wu X, Yang H, Chen J, Huang W (2012) Microstructure and mechanical properties of laser forming repaired 17-4PH stainless steel. *Materials Science and Engineering: A* 553: 80-88.
  27. Popovich V, Borisov E, Popovich AA, Sufiiarov V, Masaylo DV, Alzina L (2016) Functionally graded Inconel 718 processed by additive manufacturing: Crystallographic texture, anisotropy of microstructure and mechanical properties. *Materials & Design* 114: 10.1016/j.matdes.2016.10.075.
  28. Wang X, Liu Y, Shi T, Wang Y (2020) Strain rate dependence of mechanical property in a selective laser melted 17–4 PH stainless steel with different states. *Materials Science and Engineering: A* 792: 139776.
  29. Clausen B, Brown DW, Carpenter JS, Clarke KD, Clarke AJ, Vogel SC, Bernardin JD, Spornjak D, Thompson JM (2017) Deformation behavior of additively manufactured GP1 stainless steel. *Materials Science and Engineering: A* 696: 331-340.

# Figures

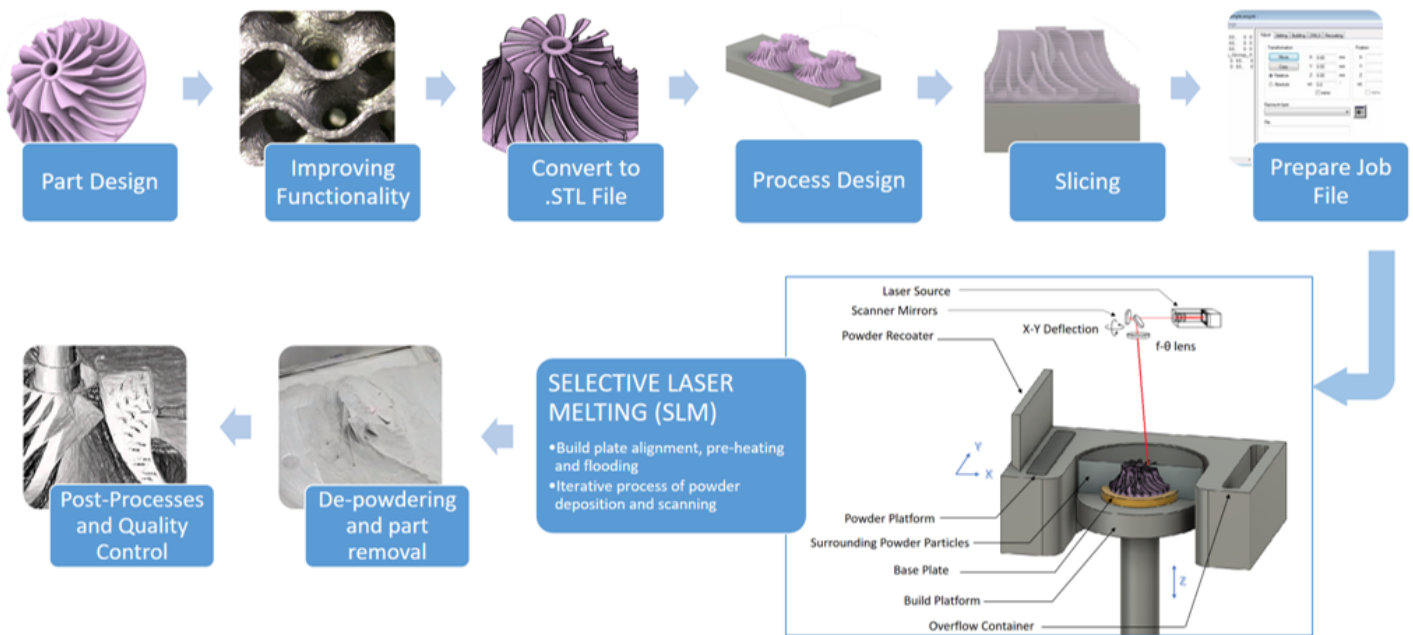


Figure 1

The process chain of Selective Laser Melting

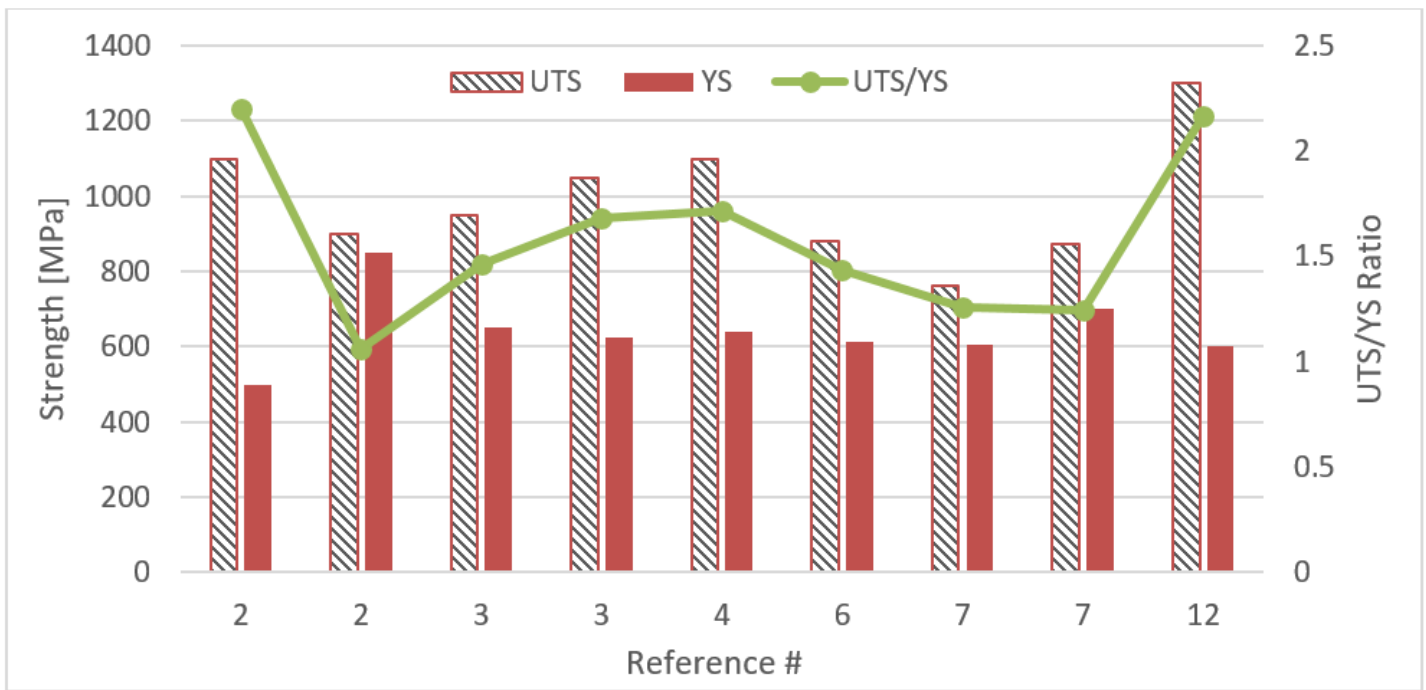
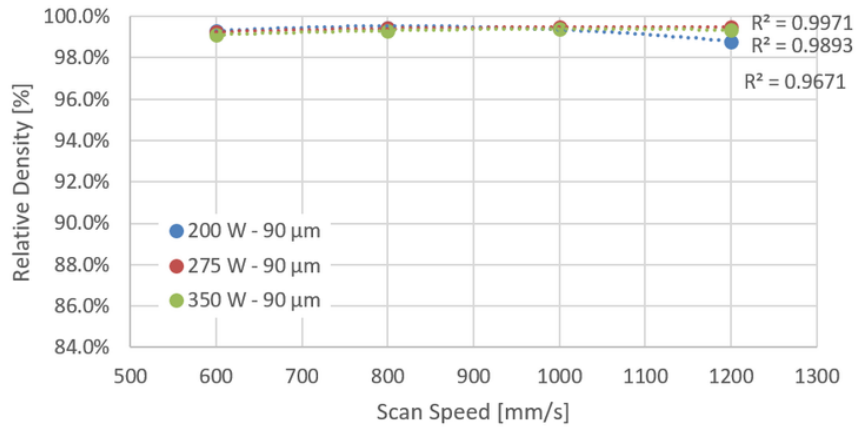
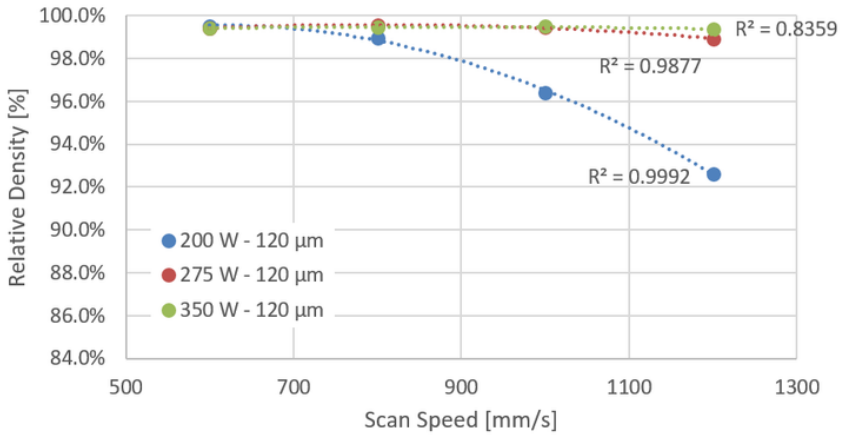


Figure 2

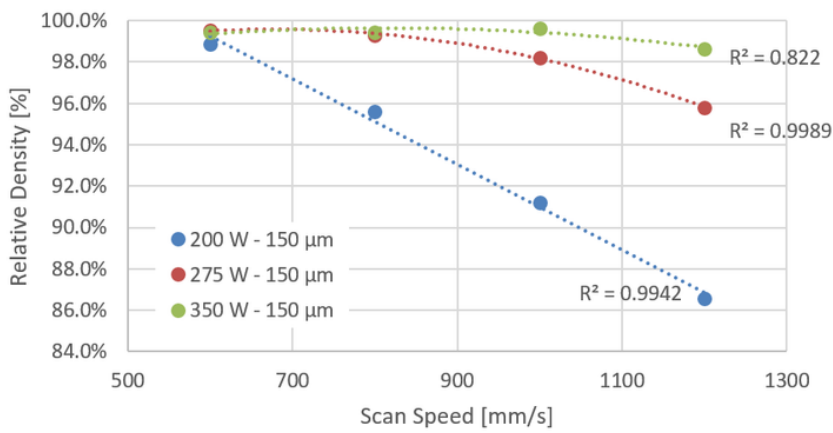
Ultimate Tensile Strength (UTS) and Yield Strength (YS) reported in various studies and UTS YS ratio



a)



b)



c)

**Figure 3**

Relative density results with respect to the scan speed (600-1200 mm/s) and laser power (200-350 W) with a hatch distance of a) 90 μm b) 120 μm c) 150 μm

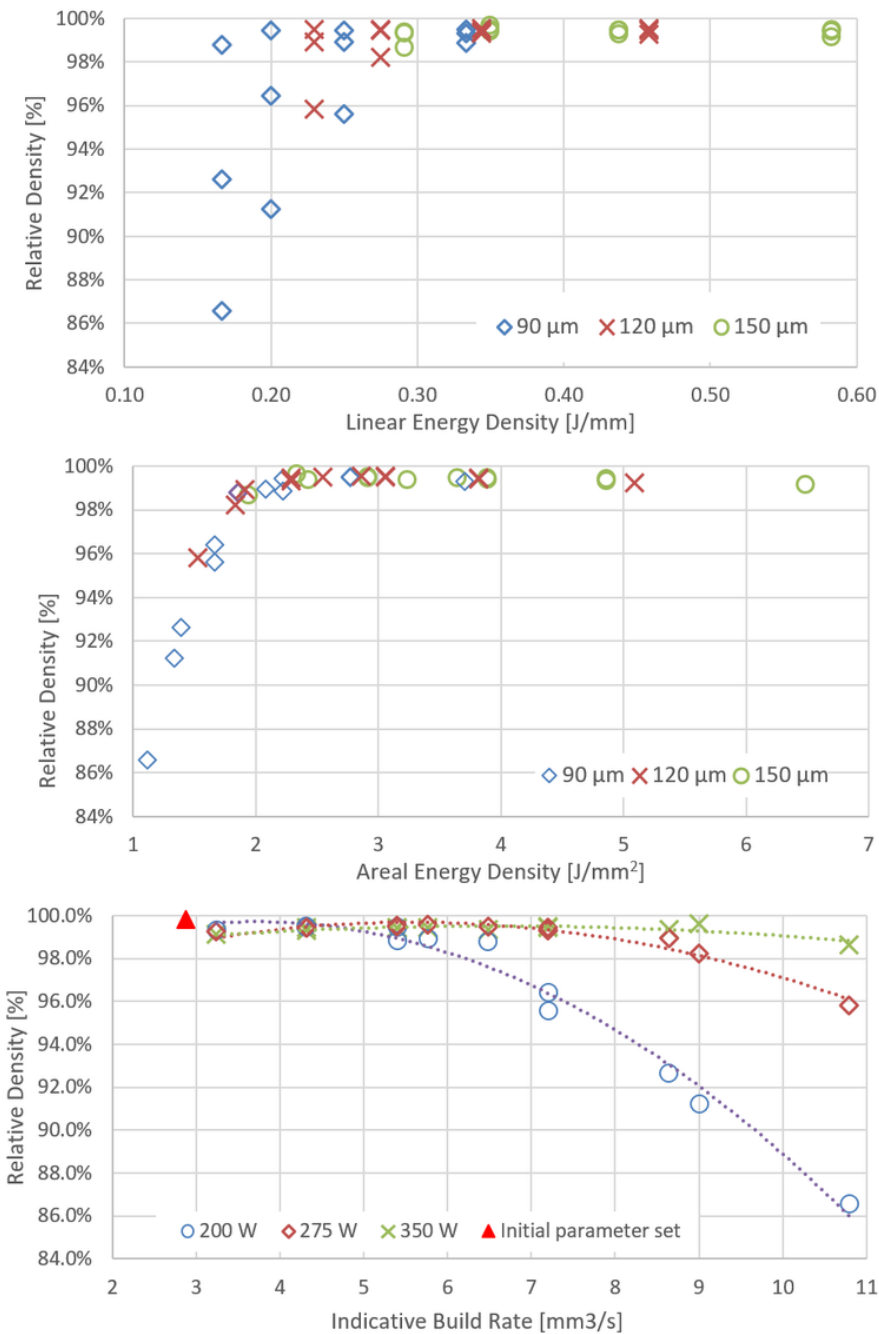


**Figure 4**

Relative density results with respect to a) linear energy density [J/mm] at different hatch distance values b) areal energy density [J/mm<sup>2</sup>] at different hatch distance values c) indicative build rate [J/mm<sup>3</sup>] at different laser power values at a layer thickness of 60 μm and the initial parameter set at a layer thickness of 30 μm

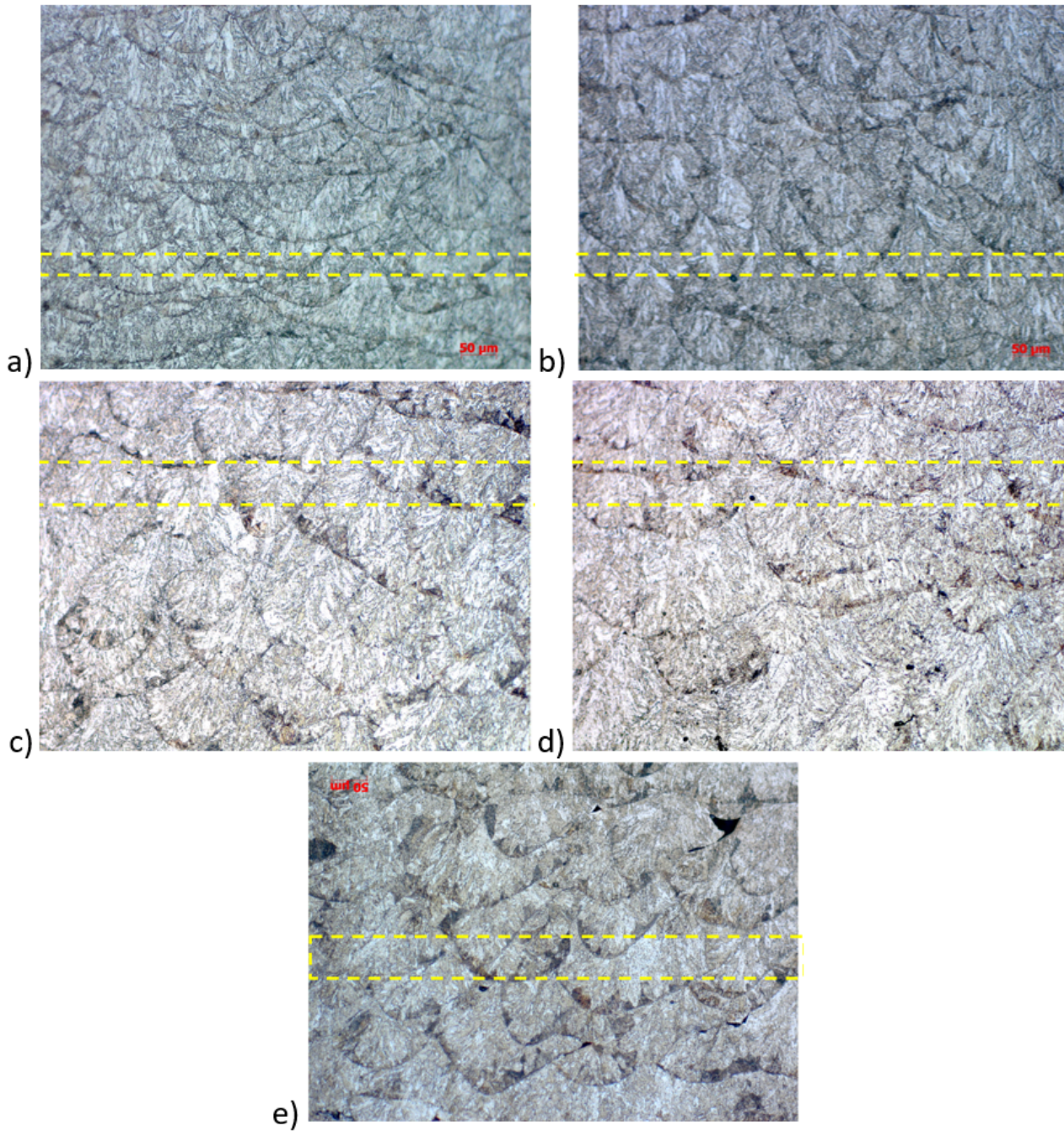


**Figure 5**

Optical microscopy images of parameter sets with 30 and 60 μm of layer thickness – one layer thickness is shown with yellow lines a) B2-St-30 b) B2-1-30 c) B-2-2-60 d) B-2-3-60 e) B2-4-60

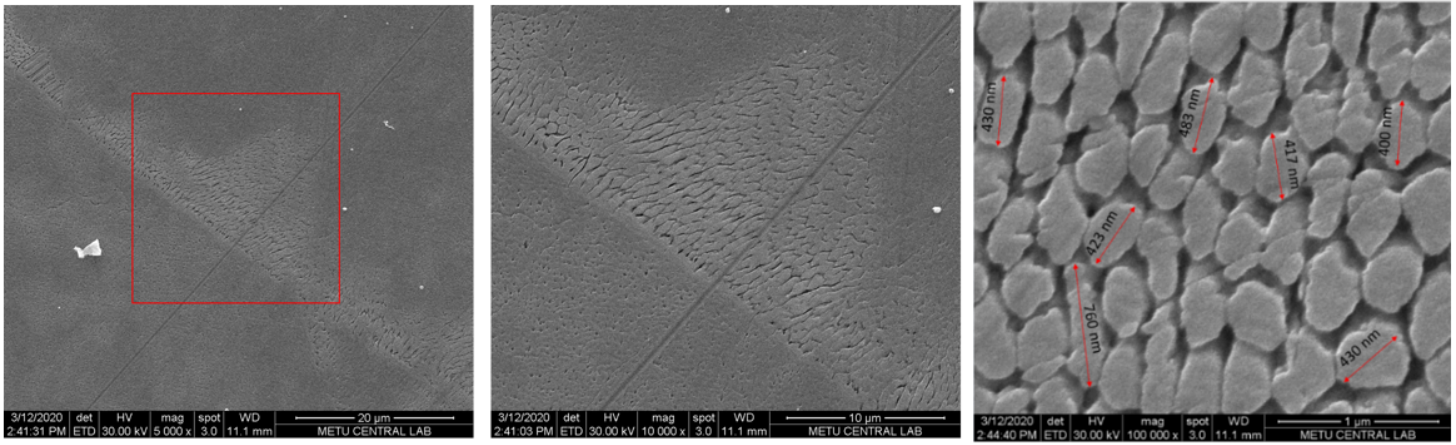


**Figure 6**

SEM images of B2-1-30 showing the cellular structure, at different magnification rates of the same area (a,b) SEM image of B2-1-30 showing the cell sizes below 1 μm (c)

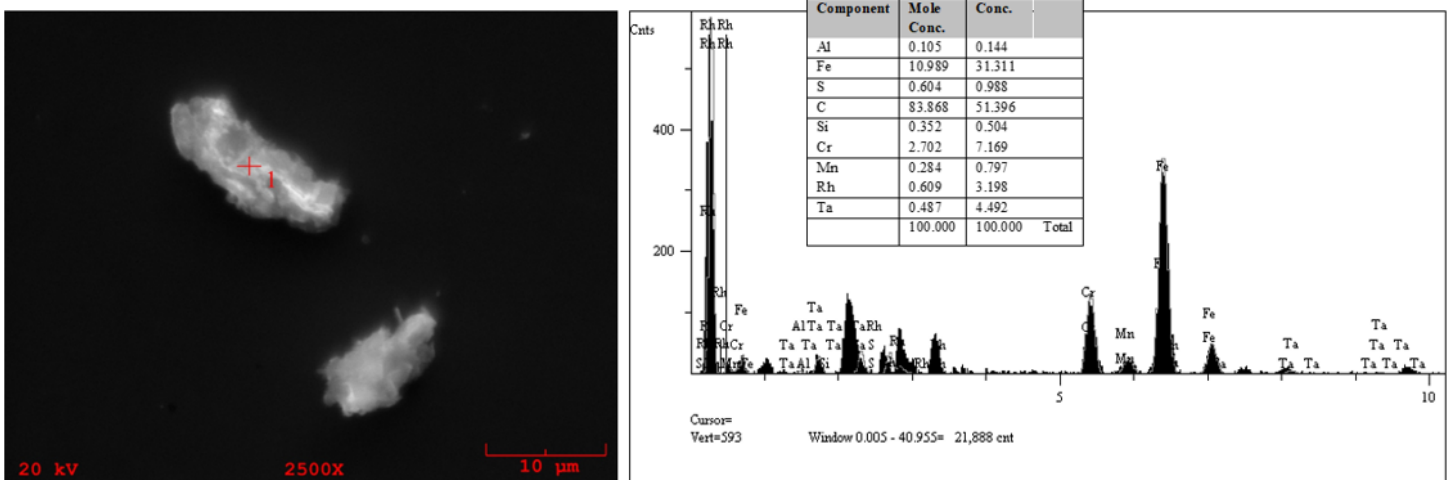
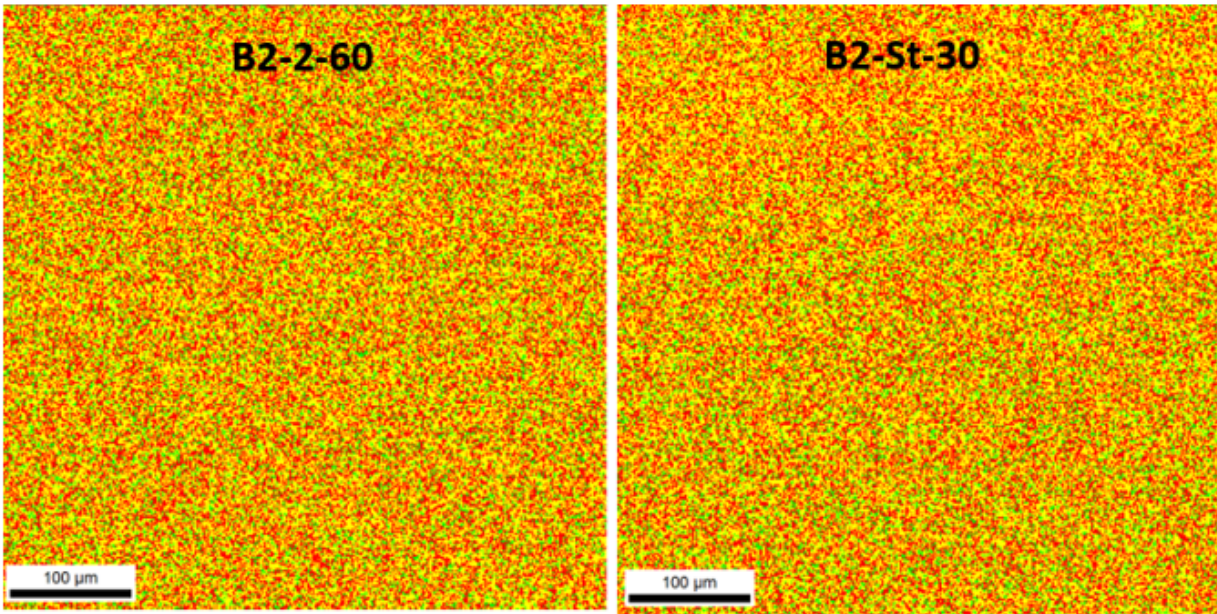


**Figure 7**

EDS analysis was performed on white spots and an example is given in this SEM image with a magnification of 2500X from B2-2-60 specimen



Phase	Total Fraction	Partition Fraction
Ferrite	0.369	0.369
Austenite	0.119	0.119
Martensite	0.512	0.512

Phase	Total Fraction	Partition Fraction
Ferrite	0.368	0.368
Austenite	0.103	0.103
Martensite	0.529	0.529

Phase	B2-2-60	B2-St-30
Ferrite	37%	41%
Austenite	9%	8%
Martensite	54%	51%

Figure 8

EBSD phase map showing ferrite, austenite and martensite for B2-St-30 and B2-2-60

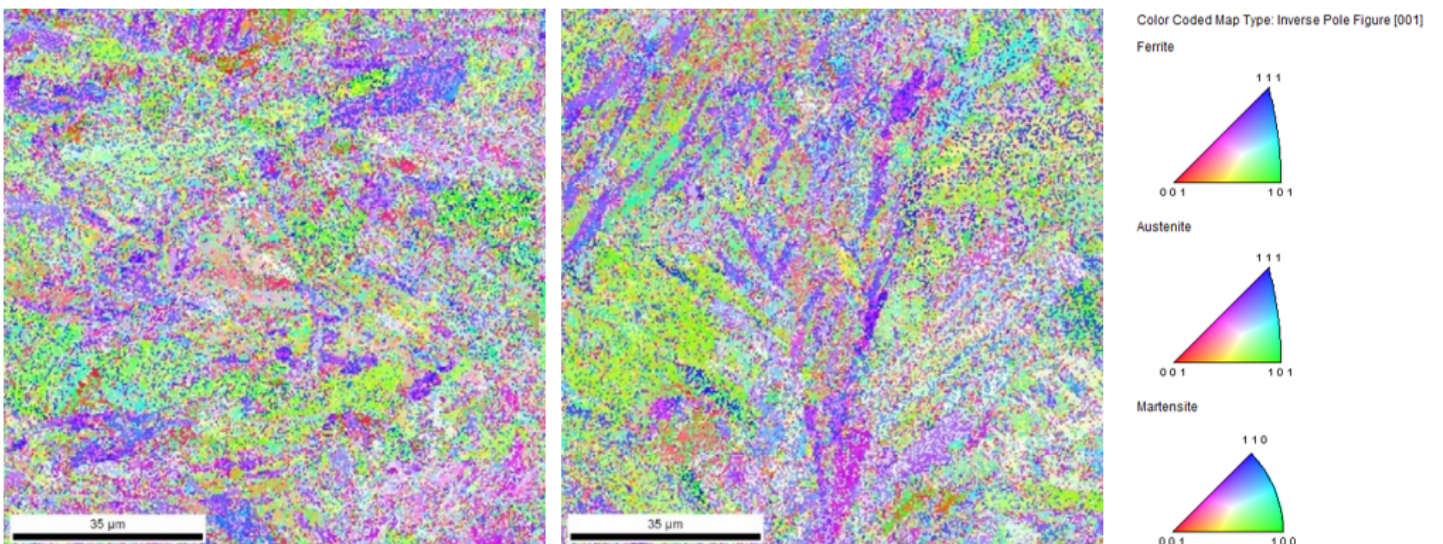
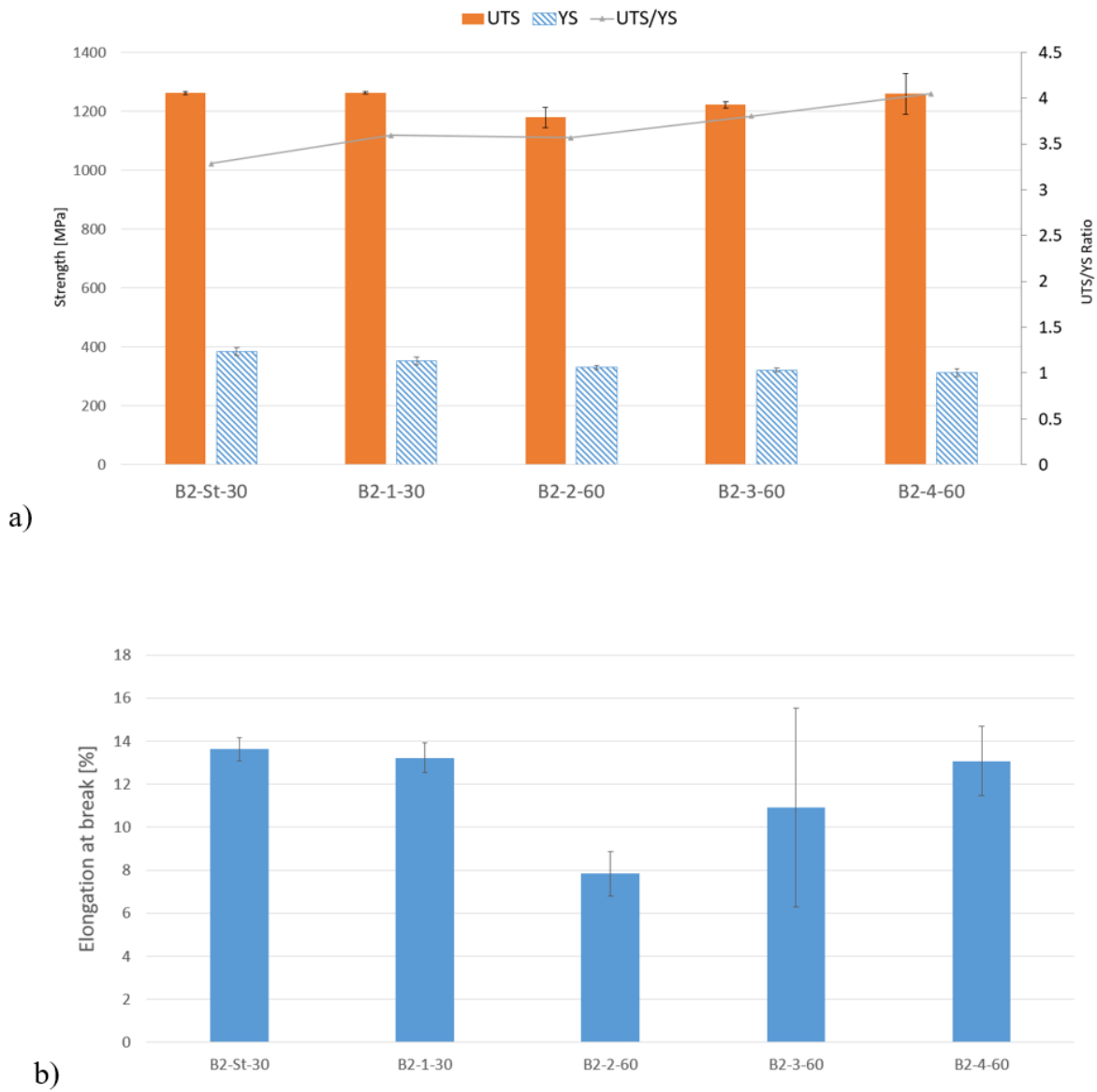


Figure 9

Inverse Pole Figures for B2-St-30 (left) and B2-2-60 (right) in the (Y-Z) plane parallel to the build direction



**Figure 10**

Tensile test results of the selected parameter sets in terms of a) UTS, YS and the ratio of UTS to YS as the secondary Y axis b) elongation at break

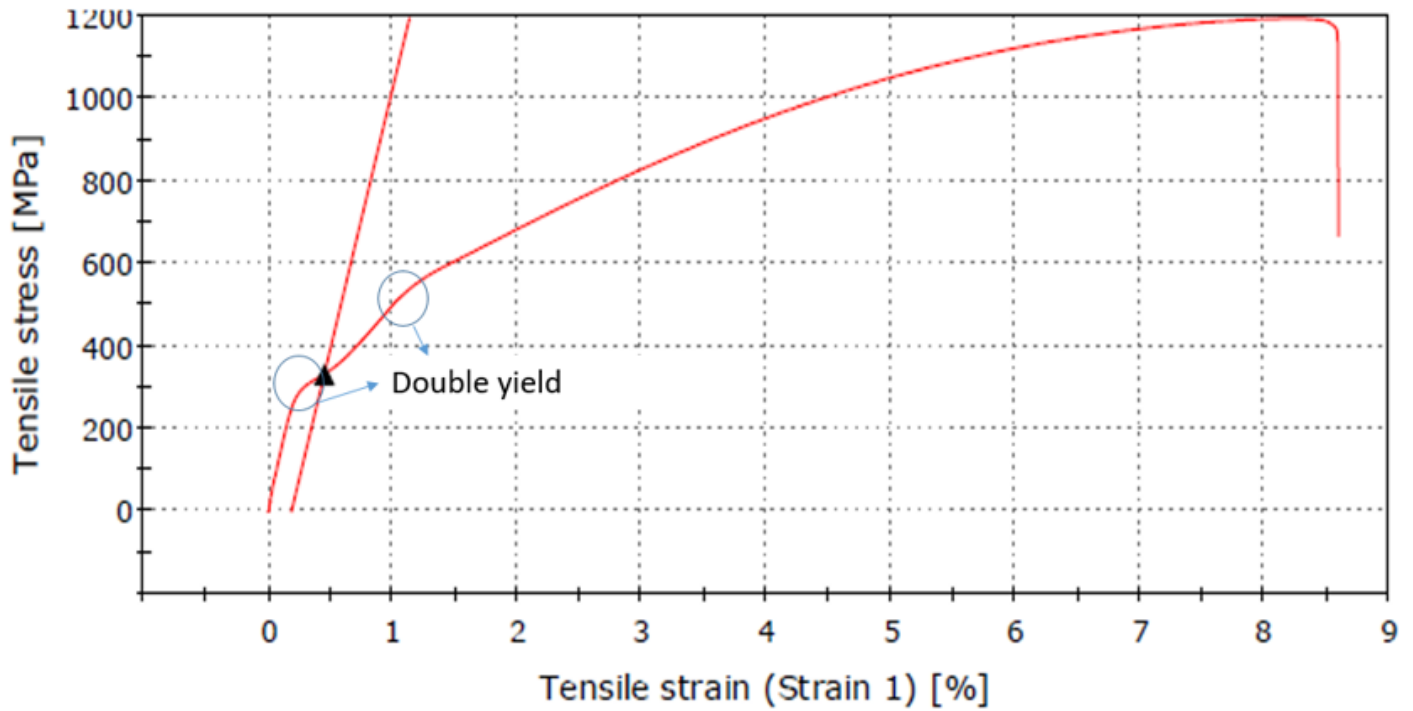


Figure 11

A representative engineering stress-strain curve from B2-2-60 specimen

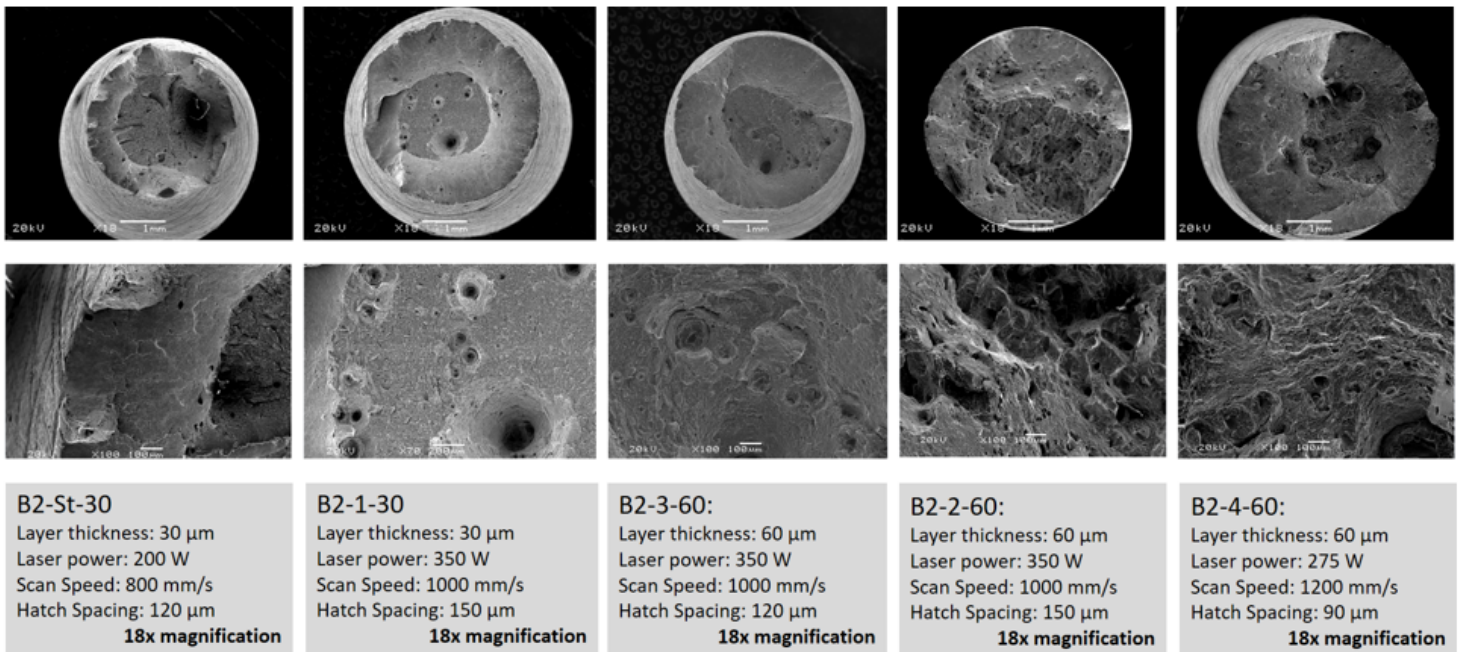


Figure 12

Scanning electron microscope (SEM) fracture morphologies from the tensile fracture surfaces